

Gate-Based Microwave Quantum Repeater Via Grid-State Encoding

Hany Khalifa * and Matti Silveri 

Nano and Molecular Systems Research Unit, University of Oulu, P.O. Box 3000, FI-90014 Oulu, Finland

In *autonomous quantum error correction* the lifetime of a logical bosonic qubit can be extended beyond its physical constituents without feedback measurements. Leveraging autonomous error correction, we propose a second-generation gate-based microwave quantum repeater (GBMQR) with encoded bosonic grid states. Each repeater station comprises a transmon and two bosonic resonators: one resonator serving as a stationary quantum memory utilizing autonomous error correction, and the other as an information bus for entanglement generation. Entanglement is generated sequentially through the successful absorption of a microwave photon wavepacket. This method enables deterministic entanglement generation, in contrast to a probabilistic mixing of two heralding signals on a balanced beamsplitter. Furthermore, our GBMQR employs an all-bosonic entanglement swapping Bell-state measurement. This is implemented via a bosonic controlled-Z gate and two separate X-basis projective homodyne measurements on the stationary stored codewords. Our approach circumvents mode-mismatch losses associated with routing and interfering of heralding modes on a beamsplitter, and confines losses to those arising from stationary storage. We evaluate the performance of the proposed quantum repeater by calculating its secret key rate under realistic lab environments. Moreover, we explicitly demonstrate that at stationary damping rate of $\kappa_{\text{damp}}^{-1} = 40 \text{ ms}$, GBMQR can achieve entanglement generation and swapping success probabilities approx. 0.75, and 0.58 respectively, surpassing the hallmark success probability of $1/2$ set by ideal linear beamsplitter-based Bell-state measurements. The proposed device can be implemented using currently available superconducting microwave technology and is suited for secure chip-to-chip communication and distributed quantum computing.

I. INTRODUCTION

The fascinating phenomenon of quantum entanglement now has the potential to enable a wide range of applications—such as *quantum key distribution* [1], *quantum teleportation* [2], *quantum sensing* [3], and many others. The efficient realization of these protocols paves the way towards achieving the long-sought goals of quantum technologies: the quantum internet [4] and distributed quantum computing [5].

Non-ideal transmissivity of a transmission medium degrades propagating quantum signals, limiting the distance over which entanglement can be reliably transmitted. Quantum repeaters [6] have evolved to overcome this limitation. The essence of a quantum repeater is to divide the original transmission distance into two segments using a middle station. In each half-channel, a pair of entangled states is generated, such that one part belongs to one of the communicating parties, while the other belongs to the middle station. After that, entanglement swapping[7] takes place by performing a *Bell-state* measurement on the two states received at the middle station. When the protocol succeeds, a final entangled state is shared between the two remote parties. This has motivated the development of three generations of quantum repeater networks. The first generation exploits quantum memories [8]. The second makes use of a highly entangled cluster state in order to eliminate the need for quantum memories [9]. The third uses encoding and error correction to achieve the same goal [10]. It is worth noting

that these technologies were not developed sequentially to improve upon each-other. Rather, they represent fundamentally different approaches, each optimized for different operational setting and constraints.

Quantum repeater technology has been developed primarily for optical-domain networking. With the emergence of highly resilient microwave *circuit quantum electrodynamics* (cQED) platforms, it is essential to adapt quantum repeater technology to the microwave domain. Although losses in microwave transmission lines are substantially higher compared to optical fibers, a microwave quantum repeater is still particularly advantageous for small-scale microwave networks, where the scalability of superconducting cQED constrains the processing power of prospective superconducting quantum computers [5]. Recent proposals have advocated a hybrid implementation via microwave-to-optical transduction to fully exploit the versatility of fiber-optic transmission lines [11]. However, highly efficient microwave-to-optical transduction at the single-photon level has yet to be demonstrated experimentally. Furthermore, the hybrid approach assumes an ideal two-photon interference Bell-state measurement realized through a balanced beamsplitter and ideal single-photon counters—devices that are currently unavailable in the microwave domain and exhibit only finite efficiency in the optical domain.

Leveraging bosonic encoding and error correction, this article proposes a *gate-based microwave quantum repeater* (GBMQR) with autonomous quantum error correction. Each repeater node comprises a transmon and two bosonic resonators, one serving as a stationary quantum memory, and the other facilitating information transfer during entanglement generation. The state of each quantum

* Corresponding author; hany.khalifa@oulu.fi

memory is encoded in a *Gottesman–Kitaev–Preskill* (GKP) grid state entangled with the transmon. This particular choice of bosonic encoding is motivated by the fact that logical operations in the codespace are performed on the resonator quadratures, making the protocol backward-compatible with legacy microwave systems. Moreover, the versatility of GKP codewords against the main sources of decoherence in the microwave domain—namely noise and losses—has been recently demonstrated [12]. In addition to that, it has been shown experimentally that the lifetime of an error-corrected GKP codeword can exceed that of an un-encoded discrete qubit state [13, 14].

Autonomous quantum error correction [13–15] is performed synchronously on all bosonic modes immediately after each memory is loaded with its GKP grid state. In this error correction method, dissipative engineering of the storage cavity implements a Hamiltonian proportional to the stabilizers of the GKP basis states, confining the codewords to the logical codespace without measuring quadratures modulo $\sqrt{\pi}$. This eliminates ancilla-induced errors associated with modular quadrature measurements.

In the entanglement generation step, the protocol utilizes an un-encoded microwave wavepacket to create entanglement *sequentially* [16]. Contrary to *concurrent* entanglement generation [17], where both a transmitter and receiver send their signals to interfere on a path-erasure balanced beamsplitter, sequential entanglement requires only one of the two communicating nodes to act as a sender. The other node implements a phase shift on the received signal, then reflects it back towards the sender to be absorbed. This approach eliminates the further damping and mode-mismatch errors associated with signal routing towards a beamsplitter. Furthermore, successful concurrent entanglement requires ideal microwave single-photon counters registering a two-mode interference-signature. Currently, efficient microwave photon number resolving detectors are not available because of the small energies in the microwave domain [18]. On the other hand, sequential entanglement is successfully achieved by implementing a deterministic absorption event. In cQED, qubit operations are now mature enough to be routinely executed in a lab environment with high fidelity and efficiency [19–21]. Thus, in this article, we assume error-free transmon operations.

Entanglement is swapped by applying a bosonic controlled-Z operation between the two middle GKP codewords. This can be achieved by a non-linear cross-Kerr coupling of the two storage resonators via a SNAIL or an additional transmon device [22, 23]. Subsequently, two projective measurements in the X-basis are performed separately on each resonator to complete the protocol. Our model uses homodyne detectors for projective measurements, which contrary to microwave photon counters are available with high efficiency [24]. As well as entanglement generation, this process realizes the required Bell-state measurement without any joint interference measurement, and hence circumvents losses due to mode-mismatch and routing through a beamsplitter device. Recently, this

method has been adapted to transfer optical noiseless linear amplifiers to the microwave domain [25, 26].

In order to quantify the performance of the proposed device, we compare the remote *secret key rate* generated by GBMQR to that of a microwave quantum repeater using a beamsplitter for entanglement generation and swapping (BSMQR) [11, 27]. Secret key analysis is performed considering device imperfections and realistic finite-energy grid states. Additionally, we demonstrate the practical conditions under which GBMQR outperforms BSMQR.

The proposed device has great potential to become a significant addition to cQED toolbox. Precisely, it can enable secure chip-to-chip communications [28], and provide entanglement-resources for microwave distributed quantum computing [29, 30], and teleportation-assisted quantum computation [31].

This article is organized as follows. Section II introduces our GBMQR by first providing a brief background of GKP grid states, followed by a detailed description of the ideal device performance. Section III considers practical limitations and imperfections of GBMQR, namely, finite-energy grid states and errors in the utilized bosonic gates. Section IV is dedicated to secret key analysis, as well as, practical performance comparison between GBMQR and BSMQR. Finally, Sec V provides conclusions and discussions.

II. GATE-BASED MICROWAVE QUANTUM REPEATER (GBMQR)

A. GKP-grid Mathematical Description

This section presents the formalism for encoding a logical GKP qubit in a single bosonic mode [32]. A bosonic mode in the Fock basis $\{|n\rangle\}$ has ladder operators a, a^\dagger , with $[a, a^\dagger] = 1$, acting as $a|n\rangle = \sqrt{n}|n-1\rangle$ and $a^\dagger|n\rangle = \sqrt{n+1}|n+1\rangle$ [33]. Equivalently, in phase space it is specified by its position quadrature $Q = (a + a^\dagger)/\sqrt{2}$, and momentum quadrature $P = (a - a^\dagger)/\sqrt{2}$, with $[Q, P] = i$, where $(\hbar = 1)$ [34], and spectral resolutions $Q = \int dz z|z\rangle_q \langle z|$, $P = \int dx x|x\rangle_p \langle x|$, where $Q|z\rangle_q = z|z\rangle_q$, $q\langle z'|z\rangle_q = \delta(z - z')$, $P|x\rangle_p = x|x\rangle_p$, and $p\langle x|x'\rangle_p = \delta(x - x')$.

Unitary phase-space dynamics of a bosonic mode are generated by the displacement $D(\lambda) = e^{\lambda a^\dagger - \lambda^* a}$ and squeezing $S(\xi) = e^{\xi a^{\dagger 2} - \xi^* a^2}$ operators, where $|\lambda|^2$ is the field intensity, and $\xi = re^{i\theta}$, such that r is the squeezing strength, and θ is the squeezing angle.

The logical qubit Pauli operations for GKP states—namely bit flip (X), phase flip (Z), and combined bit & phase flip (Y) gates—admit a representation in terms of displacement operators in the phase-space of the harmonic oscillator. We consider the square-grid GKP code [32], with $\bar{Z} = D(i\sqrt{\pi/2})$, $\bar{X} = D(\sqrt{\pi/2})$, and $\bar{Y} = i\bar{X}\bar{Z}$. The anticommutation $\{\bar{X}, \bar{Z}\} = 0$ reflects the noncommutativity of the corresponding displacement

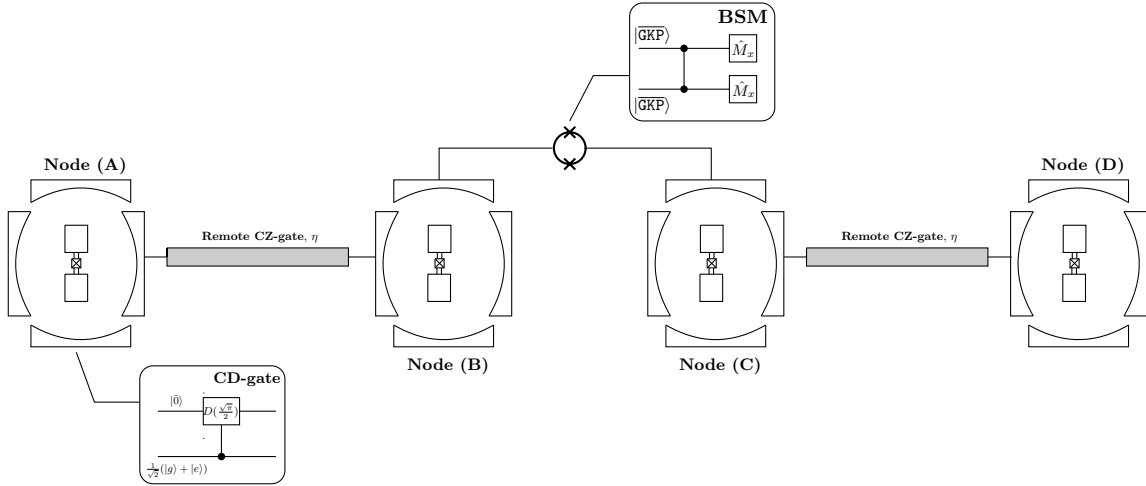


FIG. 1. A schematic of the proposed GBMQR. The figure depicts two repeater segments, where nodes A and D are the end nodes of the repeater, while B and C are located in the same place to perform a swapping operation. Each node is equipped with a transmon-two-resonator system. One resonator acts as a quantum memory loaded with a GKP codeword, while the other is coupled to a transmission line of transmissivity η that mediates remote sequential entanglement across each repeater segment. A controlled-displacement gate (CD-gate) is employed at the state preparation step as described in the main text. A swapping Bell-state measurement (BSM) is performed bosonically on the memory codewords via a controlled-Z operation followed by single bosonic-qubit measurements in the X-basis. This gate can be implemented either via an additional transmon or a SNAIL device. Ideally, the final repeater state is a bosonic Bell-state.

operators

$$[D(\lambda_1), D(\lambda_2)] = D(\lambda_2)D(\lambda_1)(e^{\lambda_1\lambda_2^* - \lambda_1^*\lambda_2} - 1), \quad (1)$$

where $\lambda_1, \lambda_2 \in \mathbb{C}$.

However, the two displacement operators commute when the phase-space area they enclose is an integer multiple of 2π (i.e., $2\pi k, k \in \mathbb{Z}_0$). Consequently, the squared logical displacements $X^2 = D(\sqrt{2\pi})$ and $Z^2 = D(i\sqrt{2\pi})$ enclose an area 4π and thus form a commuting stabilizer pair whose simultaneous +1 eigenstates define the GKP codespace.

The ideal un-normalized logical GKP codewords in the Z-basis can be written as

$$\begin{aligned} |\bar{0}\rangle &\propto \sum_{k \in \mathbb{Z}} |2k\sqrt{\pi}\rangle_q, \\ |\bar{1}\rangle &\propto \sum_{k \in \mathbb{Z}} |(2k+1)\sqrt{\pi}\rangle_q, \end{aligned} \quad (2)$$

where $\bar{Z}|\bar{0}\rangle = |\bar{0}\rangle$ and $\bar{Z}|\bar{1}\rangle = -|\bar{1}\rangle$. Analogously, the codewords in the complementary X-basis are defined as $|\tilde{0}\rangle \propto \sum_{k \in \mathbb{Z}} |2k\sqrt{\pi}\rangle_p$ and $|\tilde{1}\rangle \propto \sum_{k \in \mathbb{Z}} |(2k+1)\sqrt{\pi}\rangle_p$, where $\bar{X}|\tilde{0}\rangle = |\tilde{0}\rangle$ and $\bar{X}|\tilde{1}\rangle = -|\tilde{1}\rangle$ (see Appendix C for details).

Ideal GKP codewords are unphysical because they have infinite energy. In practice, finite-energy approximations are obtained by applying a Gaussian envelope $e^{-\Delta^2 a^\dagger a}$ to the ideal states, $e^{-\Delta^2 a^\dagger a}|\nu\rangle$, where $\nu \in \{|\bar{0}\rangle, |\bar{1}\rangle\}$ and Δ sets the envelope width [15]. This replaces the grid of δ -spikes with a superposition of centered Gaussian envelopes (see Appendix D).

B. Ideal Device Description

We now describe the ideal operation of the gate-based microwave quantum repeater. In later sections, experimental imperfections are incorporated, and device performance is assessed under practical limits.

As shown in Fig. 1, two distant repeater nodes, labeled A and D, aim to establish remote entanglement with the assistance of two intermediate nodes B and C located at the same site. The protocol involves the three archetypal steps characteristic of a quantum repeater: entanglement generation, information storage, and entanglement swapping. However, in this proposal, information storage is achieved by leveraging quantum error correction, and swapping is performed entirely on bosonic modes, taking advantage of their extended error-corrected lifetime.

At each node, a transmon-GKP state is prepared

$$|\tilde{\varphi}\rangle = \frac{1}{\sqrt{2}}(|g\rangle + |e\rangle) \otimes |\bar{0}\rangle, \quad (3)$$

where the transmon is in a superposition of its ground and excited states, while the GKP grid state is initialized in the logical-zero codeword. After that, a controlled oscillator displacement gate is applied, where the transmon acts as a control while the GKP codeword is the target [35]:

$$\begin{aligned} \mathbf{CD}|\tilde{\varphi}\rangle &= \left(|g\rangle\langle g| \otimes D\left(\sqrt{\frac{\pi}{2}}\right) + |e\rangle\langle e| \otimes \mathbb{1}_t\right)|\tilde{\varphi}\rangle \\ &= \frac{1}{\sqrt{2}}(|g\rangle_A \otimes |\bar{1}\rangle_A + |e\rangle_A \otimes |\bar{0}\rangle_A). \end{aligned} \quad (4)$$

At this point, it is assumed that all nodes are prepared in the same state as Eq. (4), and that error correction on the bosonic part is performed simultaneously at all nodes.

Our next objective is to implement a remote controlled-Z gate between nodes A and B. The overall state of the two nodes is given by

$$|\varphi\rangle_{AB} = \frac{1}{2} (|gg\rangle_{AB} \otimes |\bar{1}\bar{1}\rangle_{AB} + |ge\rangle_{AB} \otimes |\bar{1}\bar{0}\rangle_{AB} + |eg\rangle_{AB} \otimes |\bar{0}\bar{1}\rangle_{AB} + |ee\rangle_{AB} \otimes |\bar{0}\bar{0}\rangle_{AB}). \quad (5)$$

At the beginning of the gate operation a drive pulse targets the transmon part of node A at the coupling frequency of the resonator-transmission line. This step populates the transmission line with a photon temporal mode propagating towards the receiving node B [36, 37]. Accordingly, the mapping $|e\rangle|0\rangle \rightarrow |e\rangle|0\rangle$, $|g\rangle|0\rangle \rightarrow |g\rangle|1\rangle_\Gamma$ is implemented. After that, the state of the segment becomes

$$|\varphi\rangle_{AB} = \frac{1}{2} (|gg\rangle_{AB} \otimes |\bar{1}\bar{1}\rangle_{AB} \otimes |1\rangle_\Gamma + |ge\rangle_{AB} \otimes |\bar{1}\bar{0}\rangle_{AB} \otimes |1\rangle_\Gamma + |eg\rangle_{AB} \otimes |\bar{0}\bar{1}\rangle_{AB} \otimes |0\rangle_\Gamma + |ee\rangle_{AB} \otimes |\bar{0}\bar{0}\rangle_{AB} \otimes |0\rangle_\Gamma). \quad (6)$$

where $|1\rangle_\psi = \int dt \Gamma(t) a^\dagger(t) |0\rangle_\Gamma$ is a single photon temporal mode, and Γ is its temporal wavefunction (see Appendix A for details).

Upon receiving the photon wavepacket at node B, an interaction between the receiving transmon and the incoming photon is initiated. This interaction is described by the unitary $e^{-i\pi|1\rangle_{\Gamma\Gamma}\langle 1| \otimes |g\rangle_{BB}\langle g|}$ [38]. Then, the same wavepacket is reflected back towards the sending node A, where its successful absorption completes the realization of the remote controlled-Z gate. Subsequently, the state of the two nodes becomes the following:

$$|\varphi\rangle_{AB} = \frac{1}{2} (|gg\rangle_{AB} \otimes |\bar{1}\bar{1}\rangle_{AB} \otimes |0\rangle_\Gamma + |ge\rangle_{AB} \otimes |\bar{1}\bar{0}\rangle_{AB} \otimes |0\rangle_\Gamma + |eg\rangle_{AB} \otimes |\bar{0}\bar{1}\rangle_{AB} \otimes |0\rangle_\Gamma + |ee\rangle_{AB} \otimes |\bar{0}\bar{0}\rangle_{AB} \otimes |0\rangle_\Gamma). \quad (7)$$

where the gate implements the following mapping, $|g\rangle|g\rangle \rightarrow -|g\rangle|g\rangle$, $|g\rangle|e\rangle \rightarrow |g\rangle|e\rangle$, $|e\rangle|g\rangle \rightarrow |e\rangle|g\rangle$, and $|e\rangle|e\rangle \rightarrow |e\rangle|e\rangle$.

To swap the entanglement to the bosonic modes, a Hadamard transformation is applied on each transmon followed by two projective Z-basis measurements. Based on the four possible measurement outcomes, local Pauli corrections and feedforward operations are applied on the bosonic parts, such that the two remote parties share a bosonic Bell-state

$$|\Psi\rangle_{AB} = \frac{1}{\sqrt{2}} (|\bar{0}\bar{0}\rangle_{AB} - |\bar{1}\bar{1}\rangle_{AB}). \quad (8)$$

Similarly, segment C-D executes the same sequence of operations, as a result, the state of each segment is $|\Psi\rangle_{AB}$, and $|\Psi\rangle_{CD}$ respectively. Then, the overall state of the four nodes reads

$$|\Psi\rangle_{ABCD} = \frac{1}{2} (|\bar{0}\bar{0}\bar{0}\bar{0}\rangle_{ABCD} - |\bar{0}\bar{0}\bar{1}\bar{1}\rangle_{ABCD} - |\bar{1}\bar{1}\bar{0}\bar{0}\rangle_{ABCD} + |\bar{1}\bar{1}\bar{1}\bar{1}\rangle_{ABCD}). \quad (9)$$

A deterministic Bell-state measurement is now performed between nodes B and C. Using a nonlinear parametric device such as a transmon [22] or a SNAIL [23], a cross-Kerr interaction between the two modes, $e^{-iQ_B Q_C}$ [39] is applied. This introduces a negative sign only when both modes are in the logical-one state

$$|\Psi\rangle_{ABCD} = \frac{1}{2} (|\bar{0}\bar{0}\bar{0}\bar{0}\rangle_{ABCD} - |\bar{0}\bar{0}\bar{1}\bar{1}\rangle_{ABCD} - |\bar{1}\bar{1}\bar{0}\bar{0}\rangle_{ABCD} - |\bar{1}\bar{1}\bar{1}\bar{1}\rangle_{ABCD}). \quad (10)$$

After that, two X-basis measurements are performed on the middle modes yielding 4 possible outcomes. Then, the final shared state can be written as

$$|\Psi\rangle_{AD} = \frac{1}{\sqrt{2}} (|\bar{0}\bar{0}\rangle_{AD} - |\bar{1}\bar{1}\rangle_{AD}). \quad (11)$$

where, similarly as in the previous step, we apply Pauli-corrections and feedforward operations to recast the output state in the above Bell basis.

III. EXPERIMENTAL LIMITS OF GBMQR

A. Preparation Imperfections

The ideal GKP codewords cannot be realized in a laboratory setting due to finite energy constraints. Instead, a non-orthogonal, finitely squeezed pair of approximate codewords is generated. Consequently, the logical bit-flip gate becomes

$$D\left(\sqrt{\frac{\pi}{2}}\right) = \bar{X}_\Delta = |\bar{0}\rangle_{\Delta\Delta}\langle\bar{1}| + |\bar{1}\rangle_{\Delta\Delta}\langle\bar{0}|, \quad (12)$$

where the subscript Δ denotes the non-ideal gate operation. This imperfection is reflected in the working of conditional displacement, such that Eq. (4) becomes

$$\mathbf{CD}_\Delta|\varphi\rangle_\Delta = \frac{1}{\sqrt{2}} (\alpha|\bar{0}\rangle_\Delta|g\rangle + \beta|\bar{1}\rangle_\Delta|g\rangle + |\bar{0}\rangle_\Delta|e\rangle), \quad (13)$$

where $|\bar{0}\rangle_\Delta$ and $|\bar{1}\rangle_\Delta$ denote the approximate codewords and the coefficients are given by the overlaps $\alpha = {}_\Delta\langle\bar{1}|\bar{0}\rangle_\Delta$ and $\beta = {}_\Delta\langle\bar{0}|\bar{1}\rangle_\Delta$. The cross-overlap α is a measure of the code distance, whereas the similar overlap β quantifies how much logical information is preserved. The detailed expressions are given in in Appendix D.

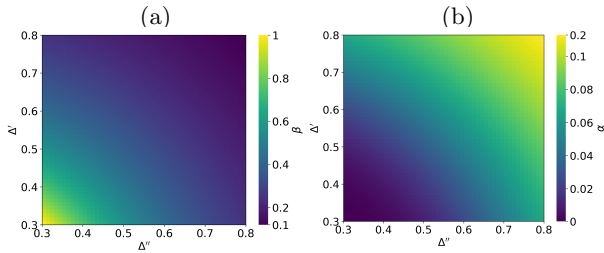


FIG. 2. Overlap between two logical GKP codewords when each is subjected to a different loss channels (Appendix D 1). Panel (a) considers the similar overlap $\beta = \Delta' \langle \bar{0} | \bar{0} \rangle_{\Delta''} = \Delta' \langle \bar{1} | \bar{1} \rangle_{\Delta''}$ as a function of Δ' and Δ'' , whereas in panel (b) the cross-overlap $\alpha = \Delta' \langle \bar{0} | \bar{1} \rangle_{\Delta''} = \Delta' \langle \bar{1} | \bar{0} \rangle_{\Delta''}$ is considered. The initial lossless variance of the codewords was assumed $\Delta = 0.3$. Ideally, when no losses are incurred, codewords are orthogonal, $\alpha = 0$, and normalized, $\beta = 1$. In the limit of large losses, $\alpha \rightarrow 1$, this implies that the code distance became zero. Consequently, the robustness of the code to losses, i.e. $\beta \rightarrow 0$ vanishes, as well as the code itself.

B. Transmission Losses

Practical transmission lines have a finite transmissivity. Therefore, an entanglement-mediating photon wavepacket incurs losses during transmission. This can be modeled by re-expressing the photon temporal wavepacket as

$$|\tilde{1}\rangle_{\Gamma} = \sqrt{\eta}|1\rangle_{\Gamma} + \sqrt{1-\eta}|0\rangle_v, \quad (14)$$

where η is the transmissivity of the channel and $|0\rangle_v$ is a vacuum environment mode, more details in Appendix B.

Since the operation of the remote controlled-Z gate is conditioned on the successful absorption of a transmitted wavepacket after undergoing a round-trip between the two cavities, entanglement between the two nodes within the same repeater segment is only established in the subset of events where the photon is successfully received back at the original transmitting cavity. This is due to the fact that when the photon is lost, the sequence of applied control pulses drives a receiving transmon outside the subset of its Hilbert space that defines the operation of the repeater. Detailed state evolution under channel losses is found in Appendix E.

C. Errors in Swapping Operation

The following step is to perform a bosonic swapping operation on the two middle GKP grid states. Swapping non-idealities are manifest as recasting the controlled-Z gate in the finite-energy GKP basis (Appendix F), and non-ideal projective homodyne measurements in the X-basis (Appendix F 1). The main sources of error in both operations are the finite overlap between logical codewords, the accumulated stationary losses due to error correction rounds, and measurement fidelity of projective measurements. Experimentally, stationary damping

rate is approximately $\kappa_{\text{damp}}^{-1} \approx 25\text{-}40 \text{ ms}$ with autonomous quantum error correction for GKP states [32]. For an initial squeezing variance of $\Delta = 0.3$, similar codeword overlap β and cross-overlap α (see Fig. 2) are calculated as $\beta \approx 0.80\text{-}0.90$, and $\alpha \approx 4 \times 10^{-4}\text{-}1 \times 10^{-3}$. As shown in Appendix F, the controlled-Z gate succeeds with a probability of $\approx \beta^2$. The measurement fidelity of a homodyne projective measurement as recently reported can reach values as high as 0.95–0.99 [24], with the assistance of digital optimization methods. Thus, for the assumed accumulated damping due to multiple error correction cycles, i.e., $\kappa_{\text{damp}}^{-1} \approx 25\text{-}40 \text{ ms}$, the success probability is $\mathcal{P}_{0/1}^{\text{succ}} \approx 0.95$ for both logical codewords. This comes from the fact that the duration of one measurement cycle is 1 μs , and the total number of measurements required to achieve this success probability is $\approx 10^3$ [24].

IV. SECRET KEY ANALYSIS

One way to assess the operation of a quantum repeater is via its secret key rate. In the event of large number of transmission instances, also known as the asymptotic limit, a secret key rate can be defined as [40–42]

$$\mathcal{R} = \mathcal{P}_{\text{EG}}^{\text{succ}} \times \mathcal{P}_{\text{SW}}^{\text{succ}} \times \mathcal{R}_{\text{raw}}, \quad (15)$$

where $\mathcal{P}_{\text{EG}}^{\text{succ}}$ is the success probability of entanglement generation, $\mathcal{P}_{\text{SW}}^{\text{succ}}$ is the success probability of entanglement swapping, and \mathcal{R}_{raw} is the raw key rate.

The raw key rate measures the fidelity of the final shared entangled state. It is defined via the quantum bit-error probability as

$$\mathcal{R}_{\text{raw}} = 1 - h(E_x) - h(E_z), \quad (16)$$

where $h(p) = -p \log(p) - (1-p) \log(1-p)$ is the binary entropy function, E_x is the bit-error rate in the X-basis, whereas E_z is the bit-error rate in the Z-basis. Bit errors arise when the detection events at the remote communicating parties, A and D (Fig. 1), correspond to a different Bell-state other than the desired one. Assuming symmetric error rates in both X and Z basis, and equal probability of projecting onto any of the other three Bell-states, the raw key rate can be recast as

$$\mathcal{R}_{\text{raw}} = 1 - 2h(E), \quad (17)$$

where $E = 2/3(1 - \mathcal{F})$, and \mathcal{F} is the fidelity between the final shared state and the ideal Bell-basis state.

A. Key Rates of GBMQR vs BSMQR

From Eq. (15), the practical performance analysis of GBMQR is evaluated. We mainly focus on the success probability of entanglement generation and swapping. A comparison is made between GBMQR and BSMQR, where the hardware efficiency of our device is demonstrated by generating higher key rate.

In a BSMQR, both entanglement generation and swapping rely on interfering two identical logical GKP wavefunctions on a balanced beamsplitter. Due to *Hong-Ou-Mandel* (HOM) interference of the codewords [43], the joint output state of the interfered modes is projected onto the *singlet* Bell-state.

Ideally, a successful Bell-state measurement happens when both of the two detectors, each placed at one of the two output ports of the beamsplitter, register no coincidence events. An important requirement for observing this phenomenon is that the interfering modes are *indistinguishable* in every degree of freedom, and that the detectors are ideal photon number resolving detectors. This restrictive requirement is crucial for the success of this measurement setup, since it is unable to decode the Bell-basis subspace entirely, and can only recognize the singlet Bell-state [44].

Practically, mode-mismatch due to transmission delays during routing towards a beamsplitter, and different error correction rounds when one repeater segment is created before the other, decreases the indistinguishability between the interfering codewords [45]. In a BSMQR this will affect the success probability of both entanglement generation and swapping. Furthermore, recent experimental implementation of a microwave beamsplitter-based Bell-state measurement was only successful with high efficiency at the single-photon level [46]. However, when multiphoton states were considered the HOM visibility dropped significantly, suggesting a similar behavior for our GKP codewords, which on the average have approx. 3–4 photons.

To model this effect we assumed two different loss channels of transmissivities η_1 and η_2 acting on each codeword separately and calculated their cross and similar overlaps α , and β , respectively. For details see Appendix D 1. When $\eta_1 = \eta_2 = 0.6$, the similar overlap was calculated as ≈ 0.34 . This value of the transmissivities corresponds to cryogenic transmission losses of 2 dB km^{-1} as recently reported [47]. Since a beamsplitter-based Bell-state measurement can only identify the singlet subspace $\{|\Psi^\pm\rangle\}$ and cannot recognize which one of the two states was detected, the success probability is upper-bounded to $1/2$ when no coincidences are registered. As a result, the final success probability of beamsplitter-based entanglement generation per repeater segment is $\mathcal{P}_{\text{EG}}^{\text{succ}} \approx 0.17$. A similar success probability is expected for entanglement swapping.

We have also considered an ideal BSMQR with higher theoretical transmissivities, $\eta_1 = \eta_2 = 0.95$. Correspondingly, the success probability of entanglement generation increases to $\mathcal{P}_{\text{EG}}^{\text{succ}} = 0.32$. This choice of the transmissivities is motivated by the fact that for a multiphoton state the HOM visibility of a beamsplitter-based setup was reported to be approx. 0.82 [46]. As before, entanglement swapping succeeds with a similar probability.

Performance Parameter	GBMQR $\kappa_{\text{damp}}^{-1} = 40\text{ms}$ $\eta = 0.60$	GBMQR $\kappa_{\text{damp}}^{-1} = 25\text{ms}$ $\eta = 0.60$	BSMQR $\eta_1 = \eta_2 = 0.95$	BSMQR $\eta_1 = \eta_2 = 0.60$
α	4×10^{-4}	10×10^{-4}	1×10^{-2}	5×10^{-2}
β	0.90	0.80	0.64	0.34
$\mathcal{P}_{\text{EG}}^{\text{succ}}$	0.75	0.60	0.32	0.17
$\mathcal{P}_{\text{SW}}^{\text{succ}}$	0.58	0.36	0.32	0.17

TABLE I. Performance parameters of GBMQR and BSMQR. The codewords cross-overlap and similar overlap are denoted α , and β respectively. The transmissivity of the channel of the remote controlled-Z gate is η , where we assumed a corresponding losses equal to 2 dB km^{-1} . Mismatch losses for each codeword are denoted η_1 , and η_2 . Stationary losses $\kappa_{\text{damp}}^{-1}$ for GBMQR are in the range of 25–40 ms. In ideal BSMQR $\eta_1 = \eta_2 = 0.95$, whereas in realistic BSMQR $\eta_1 = \eta_2 = 0.6$.

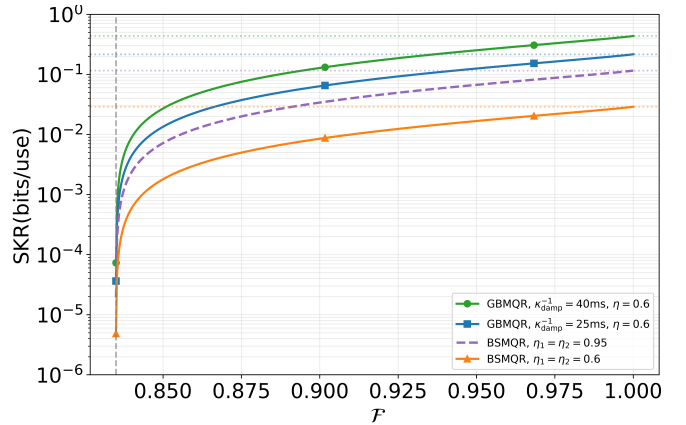


FIG. 3. A comparison between GBMQR and BSMQR secret key rates as a function of the fidelity \mathcal{F} of the final entangled state. The plot considers the fidelity threshold where a quantum repeater is capable of generating a positive key rate [41]. The best performance of GBMQR is achieved when stationary damping is $\kappa_{\text{damp}}^{-1} = 40 \text{ ms}$ (solid green). For stationary damping rate of $\kappa_{\text{damp}}^{-1} = 25 \text{ ms}$ (solid blue) GBMQR still outperforms an ideal BSMQR at overall losses of $\eta_1 = \eta_2 = 0.95$ (dashed purple). Realistic BSMQR generates the smallest secret key rate (solid orange).

On the other hand, for the operation of GBMQR we have considered errors due to stationary damping of the codewords, and gate errors in both sequential entanglement generation and entanglement swapping. We assert again here that our device mitigates mismatch errors by circumventing losses due to two-mode interference Bell-state measurements, and hence only stationary losses are dominant. This is a powerful advantage of our GBMQR over BSMQR.

In entanglement generation, by assuming ideal transmission measurements, the derived expressions for the similar and different measurement outcomes show a dependence on the transmissivity of the channel η [48, 49], and the similar overlap between logical codewords, β , due to energy truncation, and stationary damping. For a damping rate of $\kappa_{\text{damp}}^{-1} \approx 25 \text{ ms}$, and transmission losses of approx. 2 dB km^{-1} , i.e., transmissivity of $\eta = 0.6$

[47], the success probability of sequential entanglement is $\mathcal{P}_{\text{EG}}^{\text{succ}} \approx 0.60$. However, when stationary damping decreases to $\kappa_{\text{damp}}^{-1} = 40 \text{ ms}$, sequential entanglement succeeds with higher probability $\mathcal{P}_{\text{EG}}^{\text{succ}} \approx 0.75$ (detailed expressions in Appendix E).

As for entanglement swapping in GBMQR, a Bell-state measurement is achieved by a deterministic controlled-Z gate followed by two single bosonic-qubit measurements in the X-basis with local Pauli corrections and feedforward. Based on the outcomes of these measurements the system follows a deterministic trajectory towards a Bell-state. Contrary to a beamsplitter Bell-state measurement where the system follows a heralded probabilistic path that depends on detection statistics.

The success probability of the gate-based approach depends on the success probability of the entangling controlled-Z gate and the two projective measurements on the intermediate bosonic modes in the X-basis. The success probability of the projective measurements involves the measurement fidelity of a homodyne POVM detector. The controlled-Z gate has a success probability that approximately scales as the squared overlap β^2 (see Appendix F). When $\kappa_{\text{damp}}^{-1} = 25 \text{ ms}$, the overlap is $\beta \approx 0.80$, whereas when $\kappa_{\text{damp}}^{-1} = 40 \text{ ms}$, $\beta \approx 0.90$ (see Appendix D and Fig. 2). In both cases, the measurement fidelity of a homodyne detection is taken to be ≈ 0.95 . Accordingly, entanglement swapping success probability is $\mathcal{P}_{\text{SW}}^{\text{succ}} \approx 0.36$, and ≈ 0.58 respectively. It is worth noting, that the considered damping rates correspond to 150–300 rounds of error correction, each of which lasts for $\approx 7 \mu\text{s}$. Knowing that the overall duration of a typical quantum repeater protocol is in the range of 1–3 ms [6], these values reasonably estimate the overall losses.

In Fig. 3 we compare the secret key rate of both GBMQR and a beamsplitter-based microwave quantum repeater. As can be seen from the figure, the best performance was achieved by GBMQR operating at damping rate $\kappa_{\text{damp}}^{-1} = 40 \text{ ms}$. When $\kappa_{\text{damp}}^{-1} = 25 \text{ ms}$, GBMQR is able to outperform an ideal beamsplitter-based microwave repeater and generate higher key rates. Realistic beamsplitter-based microwave repeater operating at transmissivities of $\eta_1 = \eta_2 = 0.6$ generates the least secret key rate.

V. CONCLUSION

In this article we proposed a novel gate-based microwave quantum repeater (GBMQR) suitable for secure chip-to-chip communications and distributed quantum computing. Our proposed device is engineered to directly tackle the problem of probabilistic entanglement generation and swapping using a balanced beamsplitter, and to circumvent the effect of losses during information storage prior to swapping. Leveraging autonomous error correction, GBMQR takes advantage of the extended lifetime of error corrected grid states to store bosonic modes before

swapping.

Operationally, GBMQR utilizes a set of deterministic gates from the cQED toolbox. In entanglement generation, a remote transmon-transmon controlled-Z gate is utilized. For swapping, an all bosonic controlled-Z is utilized. The projective measurement required for successful entanglement generation are performed on transmons, which can be achieved with high efficiency with the available technology. Furthermore, bosonic projective measurements for entanglement swapping are performed with homodyne detectors without the need for the currently elusive microwave single photon counters. We practically evaluated the performance of GBMQR against a beamsplitter microwave quantum repeater (BSMQR) by considering their secret key rates. Since our device architecture separates stationary memory modes from propagating lossy modes, GBMQR outperformed BSMQR, due to its considerable mode mismatch and routing errors.

Some challenges remain to be resolved to enhance the performance of GBMQR. We identify two areas that can be improved to increase the fidelity of the final entangled state and, hence, the achievable key rate. First, higher channel transmissivity, η , directly increases the success probability of entanglement generation. Second, greater codeword orthogonality and more closely matched overlap β increase the success probabilities of the gates used in GBMQR. These improvements can be pursued by operating at higher squeezing levels. Currently squeezing levels as high as 10–15dB [50], introduces cross overlap errors equal to $\approx 10^{-3}$. With squeezing levels of 20dB, the errors can be suppressed further to be around $\approx 10^{-5}$.

In addition, we assume ideal transmon operations in the main text. However, errors in the operation of transmon gates would decrease the probability of successful entanglement generation. Furthermore, when the communicating chips host multiple entanglement segments and remote entanglement must be established in parallel across repeater-segment pairs, transmon crosstalk can reduce the performance of GBMQR, and decrease the final secret key rate.

Looking ahead, GBMQR could serve as a bosonic remote entangling gate that acts directly on the logical subspace of autonomously error-corrected grid states. This, in particular, would be significant when assembling bosonic square-plaquette cluster primitives into larger lattices in a nearest-neighbor, measurement-based quantum computing architecture. In this way, GBMQR can reduce long-range wiring issues that arise when compiling together long chains of cluster states. We also note that, despite physical limits on squeezing, which set the overlaps α and β and thereby the entangling gate error rate, adding an additional encoding layer on top of GKP grid states can significantly reduce error rates which is known as code concatenation.

VI. ACKNOWLEDGMENT

We acknowledge financial support from the Research Council of Finland Grant No. 359177 and the H2Future project through the Research Council of Finland (Grant. No. 352788) and the University of Oulu.

VII. AUTHOR CONTRIBUTIONS

H.K. conceived and led the research, including development of the theoretical framework, all analytical and

numerical calculations, and preparation of the manuscript. M.S. provided project supervision, funding support, and manuscript review.

[1] A. K. Ekert, Phys. Rev. Lett. **67**, 661 (1991).

[2] C. H. Bennett, G. Brassard, C. Crépeau, R. Jozsa, A. Peres, and W. K. Wootters, Phys. Rev. Lett. **70**, 1895 (1993).

[3] C. L. Degen, F. Reinhard, and P. Cappellaro, Rev. Mod. Phys. **89**, 035002 (2017).

[4] H. J. Kimble, Nature **453**, 1023 (2008).

[5] R. Van Meter and S. J. Devitt, Computer **49**, 31 (2016).

[6] N. Sangouard, C. Simon, H. de Riedmatten, and N. Gisin, Rev. Mod. Phys. **83**, 33 (2011).

[7] J.-W. Pan, D. Bouwmeester, H. Weinfurter, and A. Zeilinger, Phys. Rev. Lett. **80**, 3891 (1998).

[8] L.-M. Duan, M. D. Lukin, J. I. Cirac, and P. Zoller, Nature **414**, 413 (2001).

[9] K. Azuma, K. Tamaki, and H.-K. Lo, Nat. Commun. **6**, 6787 (2015).

[10] L. Jiang, J. M. Taylor, K. Nemoto, W. J. Munro, R. Van Meter, and M. D. Lukin, Phys. Rev. A **79**, 032325 (2009).

[11] S. S. Chelluri, S. Sharma, F. Schmidt, S. V. Kusminskiy, and P. van Loock, arXiv:2503.21569 (2025).

[12] K. Noh, S. Girvin, and L. Jiang, Phys. Rev. Lett. **125**, 080503 (2020).

[13] V. V. Sivak, A. Eickbusch, B. Royer, S. Singh, I. Tsoutsios, S. Ganjam, A. Miano, B. Brock, A. Ding, L. Frunzio, *et al.*, Nature **616**, 50 (2023).

[14] B. L. Brock, S. Singh, A. Eickbusch, V. V. Sivak, A. Z. Ding, L. Frunzio, S. M. Girvin, and M. H. Devoret, Nature **641**, 612 (2025).

[15] B. Royer, S. Singh, and S. Girvin, Phys. Rev. Lett. **125**, 260509 (2020).

[16] P. Campagne-Ibarcq, E. Zalys-Geller, A. Narla, S. Shankar, P. Reinhold, L. Burkhardt, C. Axline, W. Pfaff, L. Frunzio, R. Schoelkopf, *et al.*, Phys. Rev. Lett. **120**, 200501 (2018).

[17] A. Narla, S. Shankar, M. Hatridge, Z. Leghtas, K. M. Sliwa, E. Zalys-Geller, S. O. Mundhada, W. Pfaff, L. Frunzio, R. J. Schoelkopf, *et al.*, Phys. Rev. X **6**, 031036 (2016).

[18] M. Casariego, E. Z. Cruzeiro, S. Gherardini, T. Gonzalez-Raya, R. André, G. Frazão, G. Catto, M. Möttönen, D. Datta, K. Viisanen, *et al.*, Quantum Sci. Technol. **8**, 023001 (2023).

[19] E. J. Zhang, S. Srinivasan, N. Sundaresan, D. F. Bogorin, Y. Martin, J. B. Hertzberg, J. Timmerwilke, E. J. Pritchett, J.-B. Yau, C. Wang, *et al.*, Sci. Adv. **8**, eabi6690 (2022).

[20] W.-J. Lin, H. Cho, Y. Chen, M. G. Vavilov, C. Wang, and V. E. Manucharyan, PRX Quantum **6**, 010349 (2025).

[21] F. Marxer, J. Mrożek, J. Andersson, L. Abdurakhimov, J. Adam, V. Bergholm, R. Beriwal, C. F. Chan, S. Dahl, S. R. Das, *et al.*, arXiv:2508.16437 (2025).

[22] E. T. Holland, B. Vlastakis, R. W. Heeres, M. J. Reagor, U. Vool, Z. Leghtas, L. Frunzio, G. Kirchmair, M. H. Devoret, M. Mirrahimi, *et al.*, Phys. Rev. Lett. **115**, 180501 (2015).

[23] R. Baskov, D. K. Weiss, and S. M. Girvin, arXiv:2501.07784 (2025).

[24] I. Strandberg, A. M. Eriksson, B. Royer, M. Kervinen, and S. Gasparinetti, Phys. Rev. Lett. **133**, 063601 (2024).

[25] H. Khalifa, *Microwave quantum communications: new approaches to sensing and mitigation of the bosonic pure-loss channel*, Ph.D. thesis, Aalto University, Espoo, Finland (2024).

[26] H. Khalifa, R. Jäntti, and G. S. Paraoanu, IEEE Trans. Quantum Eng. **5**, 4100917 (2024).

[27] S. Häussler and P. van Loock, Phys. Rev. A **111**, 062611 (2025).

[28] P. Kurpiers, P. Magnard, T. Walter, B. Royer, M. Pechal, J. Heinsoo, Y. Salathé, A. Akin, S. Storz, J.-C. Besse, *et al.*, Nature **558**, 264 (2018).

[29] J. Knörzer, X. Liu, B. F. Schiffer, and J. Tura, arXiv:2510.15630 (2025).

[30] N. LaRacuente, K. N. Smith, P. Imany, K. L. Silverman, and F. T. Chong, Quantum **9**, 1581 (2025).

[31] A. P. Babu, O. Kerppo, A. Muñoz-Moller, M. Haghparast, and M. Silveri, Quantum Sci. Technol. **10**, 035004 (2025).

[32] A. L. Grimsmo and S. Puri, PRX Quantum **2**, 020101 (2021).

[33] C. C. Gerry and P. L. Knight, *Introductory quantum optics* (Cambridge university press, Cambridge, UK, 2023).

[34] D. Walls and G. J. Milburn, *Quantum Optics* (Springer, Berlin, 2025).

[35] Y. Liu, S. Singh, K. C. Smith, E. Crane, J. M. Martyn, A. Eickbusch, A. Schuckert, R. D. Li, J. Sinanan-Singh, M. B. Soley, T. Tsunoda, I. L. Chuang, N. Wiebe, and S. M. Girvin, PRX Quantum **10**, 1103/4rf7-9tfx (2025).

[36] P. Kurpiers, M. Pechal, B. Royer, P. Magnard, T. Walter, J. Heinsoo, Y. Salathé, A. Akin, S. Storz, J.-C. Besse, *et al.*, Phys. Rev. Appl. **12**, 044067 (2019).

[37] J. Ilves, S. Kono, Y. Sunada, S. Yamazaki, M. Kim, K. Koshino, and Y. Nakamura, npj Quantum Inf. **6**, 34 (2020).

- [38] Z. McIntyre and W. Coish, Phys. Rev. Research **7**, 023255 (2025).
- [39] A. Furusawa and P. Van Loock, *Quantum teleportation and entanglement: a hybrid approach to optical quantum information processing* (John Wiley & Sons, Weinheim, 2011).
- [40] N. Gisin, G. Ribordy, W. Tittel, and H. Zbinden, Rev. Mod. Phys. **74**, 145 (2002).
- [41] V. Scarani, H. Bechmann-Pasquinucci, N. J. Cerf, M. Dušek, N. Lütkenhaus, and M. Peev, Rev. Mod. Phys. **81**, 1301 (2009).
- [42] S. Pirandola, U. L. Andersen, L. Banchi, M. Berta, D. Bunandar, R. Colbeck, D. Englund, T. Gehring, C. Lupo, C. Ottaviani, J. L. Pereira, M. Razavi, J. S. Shaari, M. Tomamichel, V. C. Usenko, G. Vallone, P. Villoresi, and P. Wallden, Adv. Opt. Photon. **12**, 1012 (2020).
- [43] C.-K. Hong, Z.-Y. Ou, and L. Mandel, Phys. Rev. Lett. **59**, 2044 (1987).
- [44] G. Weihs and A. Zeilinger, in *Coherence and Statistics of Photons and Atoms*, edited by J. Peřina (Wiley, New Jersey, 2001) pp. 262–288.
- [45] F. Bouchard, A. Sit, Y. Zhang, R. Fickler, F. M. Miatto, Y. Yao, F. Sciarrino, and E. Karimi, Rep. Prog. Phys. **84**, 012402 (2020).
- [46] Y. Y. Gao, B. J. Lester, Y. Zhang, C. Wang, S. Rosenblum, L. Frunzio, L. Jiang, S. Girvin, and R. J. Schoelkopf, Physical Review X **8**, 021073 (2018).
- [47] S. Storz, J. Schär, A. Kulikov, P. Magnard, P. Kurpiers, J. Lütolf, T. Walter, A. Copetudo, K. Reuer, A. Akin, et al., Nature **617**, 265 (2023).
- [48] M. Takeoka, S. Guha, and M. M. Wilde, Nat. Commun. **5**, 5235 (2014).
- [49] S. Pirandola, R. Laurenza, C. Ottaviani, and L. Banchi, Nat. Commun. **8**, 15043 (2017).
- [50] J. Y. Qiu, A. Grimsmo, K. Peng, B. Kannan, B. Lienhard, Y. Sung, P. Krantz, V. Bolkhovsky, G. Calusine, D. Kim, et al., Nature Physics **19**, 706 (2023).
- [51] B. Brecht, D. V. Reddy, C. Silberhorn, and M. G. Raymer, Phys. Rev. X **5**, 041017 (2015).
- [52] M. Pechal, L. Huthmacher, C. Eichler, S. Zeytinoğlu, A. Abdumalikov Jr, S. Berger, A. Wallraff, and S. Filipp, Phys. Rev. X **4**, 041010 (2014).
- [53] G. Szeg, *Orthogonal polynomials*, Vol. 23 (American Mathematical Soc., 1939).
- [54] D. Gottesman, *Surviving as a quantum computer in a classical world* (Textbook manuscript preprint, 2024).
- [55] J. H. Shapiro, Quantum optical communication, MIT OpenCourseWare lecture notes (2016).
- [56] S. Glancy and E. Knill, Phys. Rev. A **73**, 012325 (2006).

Appendix A: Photon temporal basis

Temporal modes (TMs) form a complete orthonormal basis for single-photon states [51]. Although the concept of TMs can be extended to more complex photonic states, this study focuses primarily on single-photon temporal modes. Given a temporal mode shape, the wavepacket quantum state of a single-photon is defined as

$$|1\rangle_{\Gamma_n} = \int dt \Gamma_n(t) a^\dagger(t) |0\rangle_\Gamma, \quad (\text{A1})$$

where $\Gamma_n(t)$ is the complex amplitude of the temporal mode at time t , and $|0\rangle_\Gamma$ denotes the multi-mode vacuum state at different times.

The action of the creation operator a^\dagger on the multi-mode vacuum state creates a localized photon at a particular time slot t . Consequently, the single-photon wavepacket state is a coherent superposition over all possible creation times, weighted by the temporal mode function. A broadband mode operator that creates the wavepacket state $|1\rangle_{\psi_n}$ can also be defined as

$$\begin{aligned} a^\dagger[\Gamma_n] &= \int dt \Gamma_n(t) a^\dagger(t), \\ |1\rangle_{\Gamma_n} &= a^\dagger[\Gamma_n] |0\rangle_\Gamma. \end{aligned} \quad (\text{A2})$$

Furthermore, a finite orthonormal family of mode shapes $\{\Gamma\}_{m \in \mathbb{Z}}$ form a complete basis for single-photon TMs

$$\begin{aligned} \Gamma_n |1\rangle_{\Gamma_m} &= \iint dt dt' \overline{\Gamma_n(t)} \Gamma_m(t') \langle 0 | \Gamma a(t) a^\dagger(t') | 0 \rangle_\Gamma \\ &= \iint dt dt' \overline{\Gamma_n(t)} \Gamma_m(t') \delta(t - t') \\ &= \int dt \overline{\Gamma_n(t)} \Gamma_m(t) = \delta_{nm}, \quad \forall n, m \in \mathbb{Z}, \end{aligned} \quad (\text{A3})$$

where $[a(t), a^\dagger(t')] = \delta(t - t')$. One notable example of an orthonormal basis family is the set of *Hermite-Gaussian* modes, which is widely used in the optical domain.

By spanning two orthogonal mode shapes, a qubit TM can be defined as

$$|\varphi\rangle = c_0 |1\rangle_{\Gamma_0} + c_1 |1\rangle_{\Gamma_1} \quad (\text{A4})$$

where, Γ_0, Γ_1 can be taken as the two lowest-order Hermite-Gaussian functions, and $c_0, c_1 \in \mathbb{C}$. In microwave cQED, single-photon TMs have been successfully demonstrated experimentally [52], and proposed as viable information carriers for microwave quantum communications [36].

Appendix B: Pure-loss channel description

Losses due to information transfer and storage during entanglement generation and swapping are accurately described by a beamsplitter loss-channel model. In our sequential remote entanglement protocol, the degradation of the transmitted wavepacket is modeled by a unitary beamsplitter transformation that couples the transmission line input to an environment mode in its vacuum state. As a result, the output single-photon temporal mode can be expressed as

$$\begin{aligned} a[\Gamma]^{(\text{out})} &= (U_{\Gamma, v}^\theta) a[\Gamma] (U_{\Gamma, v}^\theta)^\dagger \\ &= \sqrt{\eta} a[\Gamma] + \sqrt{1 - \eta} a_v. \end{aligned} \quad (\text{B1})$$

Here, $U_{\Gamma, v}^\theta = e^{-i\theta H_{\text{BS}}}$ is the beamsplitter operator, where θ is its angle, $H_{\text{BS}} = i(a[\Gamma]^\dagger a_v + a_v a[\Gamma])$ is the corresponding

Hamiltonian. The transmissivity of the beamsplitter is given by $\cos(\theta) = \eta \in [0, 1]$. In this expression, a_v denotes the annihilation operator for the environment vacuum mode.

It is also worth noting that a beamsplitter loss channel can be represented as a 2×2 matrix .

$$\begin{pmatrix} a[\Gamma]^{(\text{out}1)} \\ a[\Gamma]^{(\text{out}2)} \end{pmatrix} = \begin{pmatrix} \sqrt{\eta} & \sqrt{1-\eta} \\ \sqrt{1-\eta} & \sqrt{\eta} \end{pmatrix} = \begin{pmatrix} a[\Gamma] \\ a_v \end{pmatrix}, \quad (\text{B2})$$

where in this case η denotes the transmissivity of the transmitting channel.

We can also define losses due to stationary damping by recasting the transmissivity of the beamsplitter as $\gamma = e^{-t/\tau}$ where t is the storage time in ms, and $\tau = \kappa_{\text{damp}}^{-1}$ is the lifetime of the stored codeword in ms. We note that here we have changed η to γ to avoid confusion with the main text.

The effect of stationary losses on the stored codewords is to increase their variance. The added variance can be calculated from the codewords position quadrature after undergoing a beamsplitter channel, $Q_{\text{out}} = \sqrt{\gamma}Q_{\text{in}} + \sqrt{1-\gamma}Q_v$, and hence the variance of the output is calculated as

$$\begin{aligned} \langle \Delta Q_{\text{out}} \rangle^2 &= \langle Q_{\text{out}}^2 \rangle - \langle Q_{\text{out}} \rangle^2, \\ \langle Q_{\text{out}}^2 \rangle &= \langle (\sqrt{\gamma}Q_{\text{in}} + \sqrt{1-\gamma}Q_v)(\sqrt{\gamma}Q_{\text{in}} + \sqrt{1-\gamma}Q_v) \rangle, \\ \langle Q_{\text{out}}^2 \rangle &= \gamma \langle Q_{\text{in}}^2 \rangle + \frac{1-\gamma}{2}, \\ \langle Q_{\text{out}} \rangle^2 &= \gamma \langle Q_{\text{in}} \rangle^2, \\ \langle \Delta Q_{\text{out}} \rangle^2 &= \gamma \langle \Delta Q_{\text{in}} \rangle^2 + \frac{1-\gamma}{2}. \end{aligned} \quad (\text{B3})$$

where $\langle Q_v \rangle = 0$.

For the stationary damping values considered in the main text we calculate their corresponding added variance as follows. When the stationary damping is 40 ms, and a storage time of 1 ms, the transmissivity becomes $\gamma = e^{\frac{-1}{40}} = 0.97$, and hence the added variance becomes 0.01. Whereas, when the stationary damping is 25 ms, the added variance is 0.02. We finally recall that the duration of a quantum repeater protocol is approx. 1–3ms.

Appendix C: GKP grid qubit: single and joint operations

Ideally, as discussed in the main text, we assume a square grid encoding. We further assume that the state of the oscillator is encoded in the Z-basis. Hence the qubit subspace is spanned by the following basis states

$$\begin{aligned} |\bar{0}\rangle &= \sum_{k \in \mathbb{Z}} |2k\sqrt{\pi}\rangle_q, \\ |\bar{1}\rangle &= \sum_{k \in \mathbb{Z}} |(2k+1)\sqrt{\pi}\rangle_q. \end{aligned} \quad (\text{C1})$$

In the continuous variable momentum basis, the position eigenkets are replaced with momentum states and the same superposition structure is preserved.

We define a logical Pauli-Z operation as $\bar{Z} = D(i\sqrt{\frac{\pi}{2}}) = e^{i\sqrt{\pi}Q}$, where $Q = (a + a^\dagger)/2$. This operator generates translations in the momentum space, whereas on a GKP basis states it acts as

$$\begin{aligned} \bar{Z}|\bar{0}\rangle &= \sum_{k \in \mathbb{Z}} e^{i\sqrt{\pi}Q} |2k\sqrt{\pi}\rangle_q = \sum_{k \in \mathbb{Z}} (e^{i2\pi})^k |2k\sqrt{\pi}\rangle_q = +1|\bar{0}\rangle, \\ \bar{Z}|\bar{1}\rangle &= \sum_{k \in \mathbb{Z}} e^{i\sqrt{\pi}Q} |(2k+1)\sqrt{\pi}\rangle_q = e^{i\pi} \sum_{k \in \mathbb{Z}} (e^{i2\pi})^k |(2k+1)\sqrt{\pi}\rangle_q \\ &= -1|\bar{1}\rangle. \end{aligned} \quad (\text{C2})$$

where $Q|z\rangle_q = z|z\rangle_q$.

On the other hand, a logical Pauli-X defined as $\bar{X} = D(\sqrt{\frac{\pi}{2}}) = e^{-i\sqrt{\pi}P}$ generates translations in position space and its action on a GKP basis is shown as

$$\begin{aligned} \bar{X}|\bar{1}\rangle &= \sum_{k \in \mathbb{Z}} e^{-i\sqrt{\pi}P} |(2k+1)\sqrt{\pi}\rangle_q \\ &= \sum_{k \in \mathbb{Z}} \int dx e^{-i\sqrt{\pi}p} |x\rangle_{pp} \langle x|(2k+1)\sqrt{\pi}\rangle_q \\ &= \frac{1}{\sqrt{\pi}} \sum_{k \in \mathbb{Z}} \int dp e^{-i\sqrt{\pi}x} e^{i\sqrt{\pi}x} e^{i2k\sqrt{\pi}x} |x\rangle_p \\ &= \sum_{k \in \mathbb{Z}} \int dx \frac{e^{i2k\sqrt{\pi}x}}{\sqrt{\pi}} |x\rangle_p \\ &= \sum_{k \in \mathbb{Z}} |2k\sqrt{\pi}\rangle_q = |\bar{0}\rangle, \\ \bar{X}|\bar{0}\rangle &= \sum_{k \in \mathbb{Z}} \int dx e^{-i\sqrt{\pi}p} |x\rangle_{pp} \langle x|2k\sqrt{\pi}\rangle_q \\ &= \sum_{k \in \mathbb{Z}} \int dx \frac{e^{i(2k-1)\sqrt{\pi}x}}{\sqrt{\pi}} |x\rangle_p \\ &= \sum_{k \in \mathbb{Z}} |(2k+1)\sqrt{\pi}\rangle_q = |\bar{1}\rangle, \end{aligned} \quad (\text{C3})$$

where $\frac{e^{ixz}}{\sqrt{2\pi}} = {}_p\langle x|z\rangle_q$, $\int dx |x\rangle_{pp} \langle x| = \mathbb{1}$, $|z\rangle_q = \frac{1}{\sqrt{2\pi}} \int dx e^{ixz} |x\rangle_p$, and we have exploited translation invariance of the infinite grid state.

The anti-commutation relation between the logical qubit Pauli operations is straightforwardly derived as

$$\begin{aligned} \bar{X}\bar{Z} &= e^{-i\sqrt{\pi}P} e^{i\sqrt{\pi}Q} \\ &= e^{i\sqrt{\pi}Q} e^{-i\sqrt{\pi}P} e^{[-i\sqrt{\pi}P, i\sqrt{\pi}Q]} \\ &= e^{i\pi} \bar{Z}\bar{X} = -\bar{Z}\bar{X}, \end{aligned} \quad (\text{C4})$$

where $e^{A+B} = e^A e^B e^{\frac{-1}{2}[A,B]} = e^B e^A e^{\frac{1}{2}[A,B]}$ was utilized.

1. Controlled-Z joint operation

A bosonic controlled-Z operation is defined as $e^{-iQ_c Q_t}$. The action of the gate on logical states is shown as

$$\begin{aligned} & e^{-iQ_c Q_t} |\bar{0}\rangle_c |\bar{0}\rangle_t \\ &= e^{-iQ_c Q_t} \sum_{k \in \mathbb{Z}} |2k\sqrt{\pi}\rangle_{q_c} \otimes \sum_{k' \in \mathbb{Z}} |2k'\sqrt{\pi}\rangle_{q_t} \\ &= \sum_{k \in \mathbb{Z}} \sum_{k' \in \mathbb{Z}} (e^{-i4\pi})^{kk'} |2k\sqrt{\pi}\rangle_{q_c} \otimes |2k'\sqrt{\pi}\rangle_{q_t} = |\bar{0}\rangle |\bar{0}\rangle, \end{aligned}$$

$$\begin{aligned} & e^{-iQ_c Q_t} |\bar{0}\rangle |\bar{1}\rangle \\ &= e^{-iQ_c Q_t} \sum_{k \in \mathbb{Z}} |2k\sqrt{\pi}\rangle_{q_c} \otimes \sum_{k' \in \mathbb{Z}} |(2k'+1)\sqrt{\pi}\rangle_{q_t} \\ &= \sum_{k \in \mathbb{Z}} \sum_{k' \in \mathbb{Z}} (e^{-i2\pi})^k (e^{-i4\pi})^{kk'} |2k\sqrt{\pi}\rangle_{q_c} \otimes |(2k'+1)\sqrt{\pi}\rangle_{q_t} \\ &= |\bar{0}\rangle |\bar{1}\rangle, \\ & e^{-iQ_c Q_t} |\bar{1}\rangle |\bar{0}\rangle = |\bar{1}\rangle |\bar{0}\rangle, \end{aligned}$$

$$\begin{aligned} & e^{-iQ_c Q_t} |\bar{1}\rangle |\bar{1}\rangle \\ &= \sum_{k \in \mathbb{Z}} \sum_{k' \in \mathbb{Z}} e^{-i\pi} (e^{-i4\pi})^{kk'} (e^{-i2\pi})^k (e^{i2\pi})^{k'} \\ & \times |(2k+1)\sqrt{\pi}\rangle_{q_c} \otimes |(2k'+1)\sqrt{\pi}\rangle_{q_t} = -|\bar{1}\rangle |\bar{1}\rangle, \end{aligned} \quad (\text{C5})$$

where the minus sign is only acquired when both of the inputs of the gate are in the logical-one state.

Appendix D: Finite-energy GKP codewords analytical expressions

As described in the main text, the finite-energy GKP code words are defined as

$$\begin{aligned} |\bar{0}\rangle_{\Delta} &= e^{-\Delta^2 \hat{n}} |\bar{0}\rangle, \\ |\bar{1}\rangle_{\Delta} &= e^{-\Delta^2 \hat{n}} |\bar{1}\rangle, \end{aligned} \quad (\text{D1})$$

where $|\bar{0}\rangle \propto \sum_{k \in \mathbb{Z}} |2k\sqrt{\pi}\rangle_q$, and $|\bar{1}\rangle \propto \sum_{k \in \mathbb{Z}} |(2k+1)\sqrt{\pi}\rangle_q$. To show the effect of applying an envelope operator, $e^{-\Delta^2 \hat{n}}$, the ideal code words are expanded in the complete or-

thonormal Fock-basis:

$$\begin{aligned} e^{-\Delta^2 \hat{n}} |\bar{0}\rangle &= \sum_{n \in \mathbb{Z}_0^+} e^{-\Delta^2 n} |n\rangle \langle n| |\bar{0}\rangle \\ &= \sum_{n \in \mathbb{Z}_0^+} e^{-\Delta^2 n} \sum_{k \in \mathbb{Z}} \langle n | 2k\sqrt{\pi} \rangle_q |n\rangle \\ &= \sum_{n \in \mathbb{Z}_0^+} \sum_{k \in \mathbb{Z}} \frac{e^{-\Delta^2 n} e^{-(2k\sqrt{\pi})^2/2}}{\pi^{1/4} \sqrt{2^n n!}} H_n(2k\sqrt{\pi}) |n\rangle, \end{aligned} \quad (\text{D2})$$

$$\begin{aligned} e^{-\Delta^2 \hat{n}} |\bar{1}\rangle &= \sum_{n \in \mathbb{Z}_0^+} e^{-\Delta^2 n} |n\rangle \langle n| |\bar{1}\rangle \\ &= \sum_{n \in \mathbb{Z}_0^+} e^{-\Delta^2 n} \sum_{k \in \mathbb{Z}} \langle n | (2k+1)\sqrt{\pi} \rangle_q |n\rangle \\ &= \sum_{n \in \mathbb{Z}_0^+} \sum_{k \in \mathbb{Z}} \frac{e^{-\Delta^2 n} e^{-(2k+1)\sqrt{\pi})^2/2}}{\pi^{1/4} \sqrt{2^n n!}} H_n((2k+1)\sqrt{\pi}) |n\rangle, \end{aligned} \quad (\text{D3})$$

where $|q\rangle_q$ is a position eigenstate, $Q|q\rangle_q = q|q\rangle_q$, with a Fock-basis representation, $\langle q|n\rangle = \frac{e^{-q^2/2}}{\pi^{1/4} \sqrt{2^n n!}} H_n(q)$, such that, $H_n(q)$ is a Hermite polynomial, and Δ^2 is the variance of the Gaussian envelope introduced by the truncation process.

Because of the non-orthogonality of the truncated codewords, the overlap and cross-overlap between codewords can be calculated as

$$\begin{aligned} & \Delta \langle \bar{0} | \bar{0} \rangle_{\Delta} \\ &= \sum_{k, k' \in \mathbb{Z}} \sum_{n, m \in \mathbb{Z}_0^+} \delta_{mn} e^{-\Delta^2 (n+m)}_q \langle 2k'\sqrt{\pi} | m \rangle \langle n | 2k\sqrt{\pi} \rangle_q \\ &= \sum_{k, k' \in \mathbb{Z}} \sum_{n \in \mathbb{Z}_0^+} \left(\frac{e^{-2\Delta^2}}{2} \right)^n \frac{H_n(2k'\sqrt{\pi}) H_n(2k\sqrt{\pi})}{\sqrt{\pi} n!} \\ & \times \exp \left(\frac{-(2k'\sqrt{\pi})^2}{2} \right) \exp \left(\frac{-(2k\sqrt{\pi})^2}{2} \right) \\ &= \frac{1}{\sqrt{\pi(1-e^{-4\Delta^2})}} \sum_{k, k' \in \mathbb{Z}} \exp \left(\frac{-(2k'\sqrt{\pi})^2}{2} \right) \exp \left(\frac{-(2k\sqrt{\pi})^2}{2} \right) \\ & \times \exp \left(\frac{8k'k\pi e^{-2\Delta^2} - (4k'^2\pi + 4k^2\pi)e^{-4\Delta^2}}{1-e^{-4\Delta^2}} \right) \end{aligned} \quad (\text{D4})$$

where normalization factor is $\mathcal{N}_{\bar{0}} = \sqrt{\Delta \langle \bar{0} | \bar{0} \rangle_{\Delta}}$. Similarly

one can compute the other codeword overlaps

$$\begin{aligned}
& \Delta \langle \bar{1} | \bar{1} \rangle_{\Delta} \\
&= \sum_{k, k' \in \mathbb{Z}} \sum_{n, m \in \mathbb{Z}_0^+} \delta_{mn} e^{-\Delta^2(n+m)} q \langle (2k'+1)\sqrt{\pi} | m \rangle \langle n | (2k+1)\sqrt{\pi} \rangle_q \\
&= \sum_{k, k' \in \mathbb{Z}} \sum_{n \in \mathbb{Z}_0^+} \left(\frac{e^{-2\Delta^2}}{2} \right)^n \frac{H_n([2k'+1]\sqrt{\pi}) H_n([2k+1]\sqrt{\pi})}{\sqrt{\pi} n!} \\
&\times \exp \left(\frac{-(2k'+1)\sqrt{\pi})^2}{2} \right) \exp \left(\frac{-(2k+1)\sqrt{\pi})^2}{2} \right) \\
&= \frac{1}{\sqrt{\pi(1-e^{-4\Delta^2})}} \sum_{k, k' \in \mathbb{Z}} \exp \left(\frac{-(2k'+1)\sqrt{\pi})^2}{2} \right) \\
&\times \exp \left(\frac{-(2k+1)\sqrt{\pi})^2}{2} \right) \\
&\times \exp \left(\frac{2(2k'+1)(2k+1)\pi e^{-2\Delta^2} - ((2k'+1)^2\pi + (2k+1)^2\pi) e^{-4\Delta^2}}{1-e^{-4\Delta^2}} \right) \tag{D5}
\end{aligned}$$

where normalization is $\mathcal{N}_{\bar{1}} = \sqrt{\Delta \langle \bar{1} | \bar{1} \rangle_{\Delta}}$.

$$\begin{aligned}
& \Delta \langle \bar{1} | \bar{0} \rangle_{\Delta} \\
&= \sum_{k, k' \in \mathbb{Z}} \sum_{n, m \in \mathbb{Z}_0^+} \delta_{mn} e^{-\Delta^2(n+m)} q \langle 2k'\sqrt{\pi} | m \rangle \langle n | (2k+1)\sqrt{\pi} \rangle_q \\
&= \sum_{k, k' \in \mathbb{Z}} \sum_{n \in \mathbb{Z}_0^+} \left(\frac{e^{-2\Delta^2}}{2} \right)^n \frac{H_n(2k'\sqrt{\pi}) H_n([2k+1]\sqrt{\pi})}{\sqrt{\pi} n!} \\
&\times \exp \left(\frac{-(2k'\sqrt{\pi})^2}{2} \right) \exp \left(\frac{-(2k+1)\sqrt{\pi})^2}{2} \right) \\
&= \frac{1}{\sqrt{\pi(1-e^{-4\Delta^2})}} \sum_{k, k' \in \mathbb{Z}} \exp \left(\frac{-(2k'\sqrt{\pi})^2}{2} \right) \\
&\times \exp \left(\frac{-(2k+1)\sqrt{\pi})^2}{2} \right) \\
&\times \exp \left(\frac{4k'(2k+1)\pi e^{-2\Delta^2} - (4k'^2\pi + (2k+1)^2\pi) e^{-4\Delta^2}}{1-e^{-4\Delta^2}} \right) \\
&= \Delta \langle \bar{0} | \bar{1} \rangle_{\Delta}, \tag{D6}
\end{aligned}$$

where $\mathcal{N}_{\bar{0}\bar{1}} = \sqrt{\Delta \langle \bar{0} | \bar{0} \rangle_{\Delta} \Delta \langle \bar{1} | \bar{1} \rangle_{\Delta}}$ denotes normalization constant.

The previous derivations were performed routinely using the standard Mehler's formula [53], $\sum_{n \in \mathbb{Z}^+} \frac{H_n(x) H_n(y)}{n!} \left(\frac{z}{2} \right)^n = \frac{1}{\sqrt{1-z^2}} \exp \left(\frac{2xyz - (x^2 + y^2)z^2}{1-z^2} \right)$. Numerical values can be obtained by truncating the sums over k, k' to a finite value. Alternatively, the double sum expressions can be recast in terms of Jacobi-Theta functions [15]. However, in this paper a standard Hermite-Mehler representation, which is mathematically equivalent to the theta-function representation, was favored in order to highlight explicitly the evolution of the codewords in the Fock-basis.

1. Coupling and mode-mismatch errors

In a beamsplitter-based Bell-state measurement, two identical GKP codewords are routed to a coupling balanced beamsplitter. However, losses due to couplings, detection

inefficiency, and mode mismatch decrease the indistinguishability between the two interfering codewords. In order to quantify this error, the overlap between codewords is considered, when each is undergoing a different loss channel. For the case of two logical-zero states, the overlap becomes

$$\begin{aligned}
& \Delta \langle \bar{0} | \otimes \langle 0_c | (U^{\eta_2})^\dagger | U^{\eta_1} | 0 \rangle_b \otimes | \bar{0} \rangle_{\Delta} \\
&= \sum_{k, k' \in \mathbb{Z}} \sum_{n \in \mathbb{Z}_0^+} (\eta_1 \eta_2 e^{-2\tilde{\Delta}^2})^n \langle 2k'\sqrt{\pi} | n \rangle \langle n | 2k\sqrt{\pi} \rangle \\
&= \sum_{k, k' \in \mathbb{Z}} \sum_{n \in \mathbb{Z}_0^+} \left(\frac{e^{-2\tilde{\Delta}^2} \sqrt{\eta_1 \eta_2}}{2} \right)^n \frac{H_n(2k'\sqrt{\pi}) H_n(2k\sqrt{\pi})}{\sqrt{\pi} n!} \\
&\times \exp \left(- \frac{(2k'\sqrt{\pi})^2}{2} \right) \exp \left(- \frac{(2k\sqrt{\pi})^2}{2} \right) \\
&= \frac{1}{\sqrt{\pi(1-(e^{-2\tilde{\Delta}^2} \sqrt{\eta_1 \eta_2})^2)}} \sum_{k, k' \in \mathbb{Z}} \exp \left(- \frac{(2k'\sqrt{\pi})^2}{2} \right) \\
&\times \exp \left(- \frac{(2k\sqrt{\pi})^2}{2} \right) \\
&\times \exp \left(\frac{8\pi k k' \left(e^{-2\tilde{\Delta}^2} \sqrt{\eta_1 \eta_2} \right) - (4\pi k^2 + 4\pi k'^2) \left(e^{-2\tilde{\Delta}^2} \sqrt{\eta_1 \eta_2} \right)^2}{1 - (e^{-2\tilde{\Delta}^2} \sqrt{\eta_1 \eta_2})^2} \right), \tag{D7}
\end{aligned}$$

where $\tilde{\Delta} = \Delta + \frac{1-\eta_1}{2} + \frac{1-\eta_2}{2}$, U^{η_1} , U^{η_2} are two different beamsplitter channels defined in Eq. (B2). As for logical-1 states,

$$\begin{aligned}
& \Delta \langle \bar{1} | \otimes \langle 0_c | (U^{\eta_2})^\dagger | U^{\eta_1} | 0 \rangle_b \otimes | \bar{1} \rangle_{\Delta} \\
&= \sum_{k, k' \in \mathbb{Z}} \sum_{n \in \mathbb{Z}_0^+} (e^{-2\tilde{\Delta}^2} \sqrt{\eta_1 \eta_2})^n \langle (2k'+1)\sqrt{\pi} | n \rangle \langle n | (2k+1)\sqrt{\pi} \rangle \\
&= \sum_{k, k' \in \mathbb{Z}} \sum_{n \in \mathbb{Z}_0^+} \left(\frac{e^{-2\tilde{\Delta}^2} \sqrt{\eta_1 \eta_2}}{2} \right)^n \frac{H_n((2k'+1)\sqrt{\pi}) H_n((2k+1)\sqrt{\pi})}{\sqrt{\pi} n!} \\
&\times \exp \left(- \frac{(2k'+1)\sqrt{\pi})^2}{2} \right) \exp \left(- \frac{(2k+1)\sqrt{\pi})^2}{2} \right) \\
&= \frac{1}{\sqrt{\pi(1-(e^{-2\tilde{\Delta}^2} \sqrt{\eta_1 \eta_2})^2)}} \sum_{k, k' \in \mathbb{Z}} \exp \left(- \frac{(2k'+1)\sqrt{\pi})^2}{2} \right) \\
&\times \exp \left(- \frac{(2k+1)\sqrt{\pi})^2}{2} \right) \\
&\times \exp \left(\frac{8\pi(k+\frac{1}{2})(k'+\frac{1}{2}) \left(e^{-2\tilde{\Delta}^2} \sqrt{\eta_1 \eta_2} \right) - (4\pi(k+\frac{1}{2})^2 + 4\pi(k'+\frac{1}{2})^2) \left(e^{-2\tilde{\Delta}^2} \sqrt{\eta_1 \eta_2} \right)^2}{1 - (e^{-2\tilde{\Delta}^2} \sqrt{\eta_1 \eta_2})^2} \right) \tag{D8}
\end{aligned}$$

where $\tilde{\Delta} = \Delta + \frac{1-\eta_1}{2} + \frac{1-\eta_2}{2}$, U^{η_1} , U^{η_2} .

It is important to note here that for the purpose of this article we choose to normalize the lossy overlaps of the codewords by the lossless normalization factors defined earlier, $\mathcal{N}_{\bar{0}}$, and $\mathcal{N}_{\bar{1}}$. This approach is standard when stationary damping is in the range of 25-40 ms as treated in this manuscript [32]. However, this is not the case when losses are high as in the case of BSMQR operating at $\eta_1 = \eta_2 = 0.6$. In this case, the codewords become a statistical mixture and the environment captures too much information, rendering any recovery operation impossible [54].

Appendix E: Entanglement generation exact success probability

This section provides the exact expression of the state shared between two nodes that undergo the entanglement generation step described in the main text. Because of transmission losses, the state evolves as

$$\begin{aligned} |\varphi\rangle_{\Delta,AB} &= \frac{1}{2} \left(-\alpha^2 \eta |gg\rangle_{AB} \otimes |\bar{0}\bar{0}\rangle_{\Delta,AB} - \alpha \beta \eta |gg\rangle_{AB} \otimes |\bar{0}\bar{1}\rangle_{\Delta,AB} \right. \\ &\quad - \alpha \beta \eta |gg\rangle_{AB} \otimes |\bar{1}\bar{0}\rangle_{\Delta,AB} - \beta^2 \eta |gg\rangle_{AB} \otimes |\bar{1}\bar{1}\rangle_{\Delta,AB} \\ &\quad + \alpha \eta |ge\rangle_{AB} \otimes |\bar{0}\bar{0}\rangle_{\Delta,AB} + \beta |eg\rangle_{AB} \otimes |\bar{0}\bar{1}\rangle_{\Delta,AB} \\ &\quad + \beta \eta |ge\rangle_{AB} \otimes |\bar{1}\bar{0}\rangle_{\Delta,AB} + |ee\rangle_{AB} \otimes |\bar{0}\bar{0}\rangle_{\Delta,AB} \\ &\quad \left. + \alpha |eg\rangle_{AB} \otimes |\bar{0}\bar{0}\rangle_{\Delta,AB} \right). \end{aligned} \quad (\text{E1})$$

After projective measurements on the transmons, followed by local operations and feedforward on the bosonic parts, the state becomes

$$\begin{aligned} |\varphi^S\rangle_{\Delta,AB} &= \frac{1}{2\mathcal{N}_S} \left((1 - \eta\alpha^2) |\bar{0}\bar{0}\rangle_{\Delta,AB} - \beta^2 \eta |\bar{1}\bar{1}\rangle_{\Delta,AB} \right. \\ &\quad \left. - \alpha \beta \eta \sqrt{2} |\bar{\Psi}^+\rangle_{\Delta,AB} \right) \end{aligned} \quad (\text{E2})$$

where the normalization factor $\mathcal{N}_S = \sqrt{(1 - \eta\alpha^2)^2 + \eta^2 \beta^4 + 2\alpha^2 \beta^2 \eta^2}$ and the overlaps ${}_{\Delta} \langle \bar{0} | \bar{0} \rangle_{\Delta} = {}_{\Delta} \langle \bar{1} | \bar{1} \rangle_{\Delta} = \beta$, and ${}_{\Delta} \langle \bar{0} | \bar{1} \rangle_{\Delta} = {}_{\Delta} \langle \bar{1} | \bar{0} \rangle_{\Delta} = \alpha$. Accordingly, the density matrix of this state is

$$\begin{aligned} \rho_{\Delta,AB}^S &= \frac{1}{4\mathcal{N}_S^2} \left((1 - \eta\alpha^2)^2 |\bar{0}\bar{0}\rangle_{\Delta,AB} \langle \bar{0}\bar{0}| \right. \\ &\quad - (1 - \eta\alpha^2) \beta^2 \eta |\bar{0}\bar{0}\rangle_{\Delta,AB} \langle \bar{1}\bar{1}| \\ &\quad + (1 - \eta\alpha^2) \alpha \beta \eta \sqrt{2} |\bar{0}\bar{0}\rangle_{\Delta,AB} \langle \bar{\Psi}^+| \\ &\quad - (1 - \eta\alpha^2) \beta^2 \eta |\bar{1}\bar{1}\rangle_{\Delta,AB} \langle \bar{0}\bar{0}| \\ &\quad - (1 - \eta\alpha^2)^2 \alpha \beta \eta \sqrt{2} |\bar{\Psi}^+\rangle_{\Delta,AB} \langle \bar{0}\bar{0}| \\ &\quad + \beta^4 \eta^2 |\bar{1}\bar{1}\rangle_{\Delta,AB} \langle \bar{1}\bar{1}| + \alpha \beta^3 \eta^2 \sqrt{2} |\bar{1}\bar{1}\rangle_{\Delta,AB} \langle \bar{\Psi}^+| \\ &\quad \left. + \alpha \beta^3 \eta^2 \sqrt{2} |\bar{\Psi}^+\rangle_{\Delta,AB} \langle \bar{1}\bar{1}| + \alpha^2 \beta^2 2\eta^2 |\bar{\Psi}^+\rangle_{\Delta,AB} \langle \bar{\Psi}^+| \right). \end{aligned} \quad (\text{E3})$$

The success probability of the entanglement generation protocol is quantified by calculating the fidelity of the previous state against the target finite-energy Bell state $|\bar{\Phi}^-\rangle_{\Delta,AB} = \frac{1}{\sqrt{2}} (|\bar{0}\bar{0}\rangle_{\Delta,AB} - |\bar{1}\bar{1}\rangle_{\Delta,AB})$

$$\mathcal{F} = \text{Tr} \{ {}_{\Delta,AB} \langle \bar{\Phi}^- | \rho_{\Delta,AB}^S | \bar{\Phi}^- \rangle_{\Delta,AB} \}. \quad (\text{E4})$$

Consequently, the fidelity becomes

$$\begin{aligned} \mathcal{F} &= \frac{1}{4\mathcal{N}_S^2} \left[(1 - \eta\alpha^2)^2 \frac{(\beta^2 - \alpha^2)}{2} + \beta^2 \eta (1 - \eta\alpha^2) (\alpha^2 - \beta^2)^2 \right. \\ &\quad \left. + \frac{\beta^4 \eta^2}{2} (\alpha^2 - \beta^2)^2 \right]. \end{aligned} \quad (\text{E5})$$

As can be seen the fidelity expression is a function of the transmissivity of the channel and the overlap between the codewords.

Appendix F: Entanglement swapping practical success probability

After establishing entanglement successfully, each of the two repeater segments is in a similar bipartite state. In the finite-energy GKP basis, the overall state can be written as

$$\begin{aligned} |\bar{\Psi}\rangle_{\Delta,ABCD} &= \frac{1}{2} \left[|\bar{0}\bar{0}\bar{0}\bar{0}\rangle_{\Delta,ABCD} - |\bar{0}\bar{0}\bar{1}\bar{1}\rangle_{\Delta,ABCD} \right. \\ &\quad \left. - |\bar{1}\bar{1}\bar{0}\bar{0}\rangle_{\Delta,ABCD} + |\bar{1}\bar{1}\bar{1}\bar{1}\rangle_{\Delta,ABCD} \right]. \end{aligned} \quad (\text{F1})$$

The swapping operation proceeds by first applying a controlled-Z operation between nodes B and C, followed by a projective measurement on the two nodes in the X-basis. Device imperfections and losses are considered by recasting the involved gates in the non-orthogonal finite-energy GKP basis.

An erroneous controlled-Z gate can be written as:

$$\mathbf{CZ}_{\Delta} = |\bar{0}\rangle_{\Delta\Delta} \langle \bar{0}| \otimes \mathbf{I} + |\bar{1}\rangle_{\Delta\Delta} \langle \bar{1}| \otimes Z_{\Delta} \quad (\text{F2})$$

where $Z_{\Delta} = |\bar{0}\rangle_{\Delta\Delta} \langle \bar{0}| - |\bar{1}\rangle_{\Delta\Delta} \langle \bar{1}|$. Subsequently, the state becomes

$$\begin{aligned} |\bar{\Psi}\rangle_{\Delta,ABCD} &= \frac{1}{2} \left[\beta (|\bar{0}\bar{0}\bar{0}\bar{0}\rangle_{\Delta,ABCD} - |\bar{0}\bar{0}\bar{1}\bar{1}\rangle_{\Delta,ABCD} - |\bar{1}\bar{1}\bar{0}\bar{0}\rangle_{\Delta,ABCD} \right. \\ &\quad \left. - |\bar{1}\bar{1}\bar{1}\bar{1}\rangle_{\Delta,ABCD}) + \alpha (|\bar{0}\bar{1}\bar{0}\bar{0}\rangle_{\Delta,ABCD} + |\bar{0}\bar{1}\bar{1}\bar{1}\rangle_{\Delta,ABCD} \right. \\ &\quad \left. - |\bar{1}\bar{1}\bar{0}\bar{0}\rangle_{\Delta,ABCD} + |\bar{1}\bar{0}\bar{1}\bar{1}\rangle_{\Delta,ABCD}) \right], \end{aligned} \quad (\text{F3})$$

where as before $\beta = \langle \bar{0} | \bar{0} \rangle = \langle \bar{1} | \bar{1} \rangle$, and $\alpha = \langle \bar{0} | \bar{1} \rangle = \langle \bar{1} | \bar{0} \rangle$. The gate errors resulting in flipping the states of both the control and target qubits are second order in the cross overlap of the logical codewords α , where $\alpha \lll 1$.

1. Imperfect projective measurement in GKP basis

The next step in the swapping process is to perform two projective homodyne measurements on the middle modes. For projective homodyne detection, an operator description of this process is captured by the continuous variable positive operator-valued measure (POVM) formalism. As defined earlier, the GKP logical states adopted in this article are superpositions of the position eigenstates of the oscillator. Completeness and orthonormality in the continuous-variable setting take the following form

$$\int dk |k\rangle_{qq} \langle k| = \mathbf{1}, \quad {}_q \langle k' | k \rangle_q = \delta(k' - k). \quad (\text{F4})$$

In this representation, the position quadrature operator can be expanded in these eigenstates as

$$Q = \int dk k |k\rangle_{qq} \langle k|. \quad (\text{F5})$$

Accordingly, a set of POVMs can be defined as the set of projectors on the position eigenstates [55]

$$\hat{\Pi}(k) = |k\rangle_{qq}\langle k|. \quad (\text{F6})$$

Following directly from their definitions, it is evident that the POVM elements $\{\hat{\Pi}(k)\}_{k \in \mathbb{R}}$ are Hermitian, $\hat{\Pi}(k) = \hat{\Pi}^\dagger(k)$. Furthermore, POVMs are positive-semidefinite operators, $\langle \psi | \hat{\Pi}(k) | \psi \rangle \geq 0 \forall \psi$, which can be verified in a straight forward manner by recalling the Hermite representation of the harmonic oscillator states and their orthogonality property. Finally, the POVM elements resolve the identity $\int dk \hat{\Pi}(k) = \mathbb{1}$.

With this mathematical machinery, a projective measurement of a logical codeword and its success probability can now be feasibly defined. By considering inefficiencies of the detector, the probability of successfully detecting a logical zero state $|\bar{0}\rangle_\Delta$ can be defined as:

$$\mathcal{P}_0^{\text{succ}}(k) = \text{Tr}\{\hat{\Pi}_k U^{\tilde{\eta}} \rho_{\bar{0},\Delta} [U^{\tilde{\eta}}]^\dagger\}, \quad (\text{F7})$$

where $U^{\tilde{\eta}}$ defines a beamsplitter transformation describing losses due to detection imperfections, such that $\tilde{\eta}$ is its transmissivity.

Practically, due to the *Gaussianity* of both the initial energy truncation of the GKP codewords and losses during detection, the decision interval of a homodyne detector for the logical-zero state is centered around the zero,

i.e., $k \in [-\pi/2, \pi/2]$, and the probability of successful detection is a gaussian distribution [56]

$$\begin{aligned} \mathcal{P}_0^{\text{succ}}(k) &= \frac{1}{\sqrt{2\pi\Delta^2}} \int_{-\sqrt{\pi}/2}^{\sqrt{\pi}/2} dk e^{-k^2/2\Delta^2} \\ &= \text{erf}(\sqrt{\pi}/2/\sqrt{2\Delta}), \end{aligned} \quad (\text{F8})$$

where $\text{erf}(k) = 2/\sqrt{\pi} \int_0^k dk' e^{-k'^2}$. Similarly, the success probability of detecting a logical-one GKP codeword can be written as

$$\begin{aligned} \mathcal{P}_1^{\text{succ}}(k) &= \frac{1}{\sqrt{2\pi\Delta^2}} \int_{\sqrt{\pi}/2}^{3\sqrt{\pi}/2} dk e^{-(k-\sqrt{\pi})^2/2\Delta^2} \\ &= \text{erf}(\sqrt{\pi}/2/\sqrt{2\Delta}), \end{aligned} \quad (\text{F9})$$

where the decision is centered in this case around the peak value of logical-one GKP state. As described in the main text these success probabilities can be improved with the assistance of digital optimization methods to reach values as high as 0.95–0.99, and hence for our calculations we chose the success probability of detecting either a logical-zero or a logical-1 to be $\mathcal{P}_{0/1}^{\text{succ}} \approx 0.95$.